MADRID
inter.noise 2019
June 16 - 19
NOISE CONTROL FOR A BETTER ENVIRONMENT

Towards an efficient detection of hydrodynamic-acoustic feedback mechanisms in an industrial context

Kempf, Daniel [1]
Institute of Aerodynamics and Gas Dynamics
University of Stuttgart, Pfaffenwaldring 21,70569 Stuttgart, Germany

Munz, Claus-Dieter[2]
Institute of Aerodynamics and Gas Dynamics
University of Stuttgart, Pfaffenwaldring 21,70569 Stuttgart, Germany

ABSTRACT

Direct noise computation (DNC) offers some advantages compared to hybrid approaches in simulating aeroacoustic mechanisms. In DNC, hydrodynamics and acoustics are solved in a coupled manner which allows to depict intricate interactions between both fields. However, this approach intrinsically requires the resolution of the occurring disparate length and time-scales. Our open-source Discontinuous Galerkin framework FLEXI, has been successfully applied to this multiscale problem. The aim of this paper is to draw the attention to an efficient method for the detection of aeroacoustic feedback. Aeroacoustic feedback can be effectively predicted by a global stability analysis. Here, an impulse response analysis on a time averaged flow field is carried out. The underlying baseflow is maintained constant through volume forcing terms. To overcome the drawback of long time-averaging of LES-data, the question arises if a computationally less expensive numerical method, ideally a RANS-solver, can be employed to generate the time-averaged baseflow which is then used by FLEXI to simulate the response of small perturbations. Results of a side-view mirror will demonstrate the advantages of the latter approach. In summary, this paper will introduce an efficient method to depict aeroacoustic feedback within our framework FLEXI with regard to future industrial use.

Keywords: Aeroacoustic feedback loop, Side-view mirror, Global instability
I-INCE Classification of Subject Number: 76

[1]kempf@iag.uni-stuttgart.de
[2]munz@iag.uni-stuttgart.de

1. INTRODUCTION

The industry is already successfully using acoustic simulations in the development process. Nowadays broadband noise can be predicted well and also with high efficiency using hybrid simulation methods. Narrow band noise, which often occurs in flow around sharp-edged bodies or notches, however, cannot be depicted by the standard approaches. Therefore, up to this day the development process in industry relies strongly on empiricism and experiments. As an example concerning acoustic feedback there is the side-view mirror. With its smooth surface and the positioning within freestream condition promotes the development of tonal noise.

Several works dealing with tonal noise investigated trailing edge noise at the example of the NACA 0012 airfoil [1], [2], [3]. Lounsberry et al. [4] suggested that the tonal noise seen at smooth surfaces is based on the same mechanism. The mechanism is associated to laminar boundary layer separation and the associated coherent vortex shedding. Within the developing shear layer instabilities are amplified and eventually roll up to coherent vortices. The interaction of those structures with the trailing edge leads to acoustic radiation. The upstream travelling acoustic wave interacts with the shear layer trough receptivity and excites instabilities at a certain frequency. This mechanism can trigger a self-sustaining oscillatory state at certain frequency, which is the source of tonal noise.

The described interaction between hydrodynamics and acoustics is the reason why state of the art computational aeroacoustic solver can't predict acoustic feedback. To depict aeroacoustic feedback direct noise computation (DNC) is necessary. Frank [5] successfully demonstrated the occurrence of aeroacoustic feedback on a side-view mirror by applying DNC. However, this approach intrinsically requires the resolution of the disparate length and time-scales of non-linear turbulent production and the acoustic propagation. Furthermore, he applied a global stability analysis to detect acoustic feedback proposed by Jones et. al [3]. Here, an initial time averaged flow field obtained from compressible high-fidelity large eddy simulation (LES) is disturbed by a small perturbation, while the underlying baseflow is maintained through volume forcing terms. The whole procedure stays computationally expensive if a high-fidelity simulation is used to acquire the time-averaged baseflow since long time-averaging intervals are necessary to achieve statistical convergence. To overcome this drawback, we propose a more efficient method by the use of a less expensive numerical method, based on the Reynolds averaged Navier-Stokes equations (RANS), to generate the time-averaged baseflow. We apply this method to a simplified side-view mirror and will demonstrate the applicability of the of this approach.

This paper is structured as follows. Section 2 introduces the numerics essential for this work. Section 3 describes the numerical setup used for the simulations. Results based on this framework are discussed in the following two chapters, Section 4 and 5. Finally section 6 ends with concluding remarks.

2. NUMERICAL METHOD

The mechanism of acoustic feedback is based on an complex interaction between the hydrodynamics and the acoustics which requires a direct numerical simulation of the compressible Navier-Stokes equations (NSE). Such multiscale problems have strong requirements on the numerical scheme. In recent years, high order Discontinuous Galerkin (DG) methods have gained significant attention as baseline schemes for

multiscale problems. Due to low numerical approximation errors and excellent high-performance computing capabilities, they have been successfully applied to large multiscale simulations. However, this multi-scale problem still is very resources intensive, expensive and not feasible for large scale application in the industry.

The following sections summarizes the discontinuous Gelerkin spectral element method (DGSEM) implemented in our framework FLEXI as described in Hindelang at. al [6], the global stability analysis and briefly introduces the numerics of the underlying used FV solver.

2.1. Discontinuous Galerkin spectral element method

We consider the compressible NSE which are the governing equation for a compressible, viscous fluid in motion which intrinsically includes the hydrodynamics and acoustics. Expressed in the conservative form and written in terms of the vector of conserved quantities $U = (\rho, \rho v_1, \rho v_2, \rho v_3, \rho e)^T$, where ρ denotes the density of the fluid, $\vec{v} = (v_1, v_2, v_3)^T$ the fluid velocity vector and e the specific total energy, the NSE are

$$U_t + \vec{\nabla}_x \cdot \vec{F}(U_x, \vec{\nabla}_x U) = 0. \tag{1}$$

To numerically solve this system of equations with the DGSEM, the physical domain is discretized with three-dimensional, non-overlapping hexahedral elements. For a better representation of the geometry we use curved elements and for easier meshing we allow an unstructured mesh topology. Each element is mapped from the physical space to the unit reference element $E = [-1; 1]^3$ with coordinates $\vec{\xi} = (\xi_1, \xi_2, \xi_3)^T$. The metric terms are chosen according to Kopriva [7] to ensure the so-called free-stream preserving property. The transformed NSE reads as following

$$J(\vec{\xi})U_t + \vec{\nabla}_\xi \cdot \vec{\mathcal{F}}(U, \vec{\nabla}_x U) = 0, \tag{2}$$

where $J = det(\frac{\partial \vec{x}}{\partial \vec{\xi}})$ is the Jacobian determinant of the mapping $\vec{x}(\vec{\xi})$ and $\vec{\mathcal{F}}$ the transformed difference of advection and viscous fluxes. The variational form is obtained by projecting Equation (2) onto a test function ϕ, which is chosen in the Galerkin approach identical to the basis function. Integrating over the reference element E and integration by parts yields the weak formulation of the DGSEM

$$\frac{\partial}{\partial t}\int_E JU\phi \, d\vec{\xi} + \oint_{\partial E} (\mathcal{G}_n^* - \mathcal{H}_n^*)\phi \, ds - \int_E \vec{\mathcal{F}}(U, \vec{\nabla}_x U) \cdot \vec{\nabla}_\xi \phi \, d\vec{\xi} = 0, \tag{3}$$

where $\mathcal{G}$ and $\mathcal{H}$ denoted numerical flux function normal to the surface for the inviscid and the viscous term respectively. As basis for the solution vector we choose a tensor product of 1-D Lagrange polynomials l_i^N of degree N,

$$U(\vec{\xi}, t) = \sum_{i,j,k=0}^{N} \hat{U}_{ijk}(t)\psi_{ijk}^N(\vec{\xi}), \qquad \psi_{ijk}^N(\vec{\xi}) = \ell_i^N(\xi^1)\ell_j^N(\xi^2)\ell_k^N(\xi^3), \tag{4}$$

where $\hat{U}_{ijk}(t)$ is the time-dependent nodal degree of freedom. Using the $(N+1)^3$ Gauss-Legendre quadrature points both for integration and interpolation yields a collocation approach following Kopriva [8]. To determine the inviscid surface flux the Roe Riemann solver with entropy fix [9] is used to obtain the numerical fluxes depending on the values at the grid interface. The viscous flux is approximated by the lifting procedure by Bassi

and Rebay [10]. As time integration scheme the low storage fourth order explicit Runge-Kutta method of Carpenter and Kennedy [11] is applied.

The treatment of the boundaries is crucial when dealing with acoustics. To prevent artificial reflections of acoustic waves as well as of the turbulent flow structures we use a sponge zone proposed by Pruett [12] as well as boundary conditions of Dirichlet type in weak form. Further details about the implementation and the acoustic properties of the DGSEM can be found in Flad et. al [13].

2.2. Global perturbation simulation

To reduce computational cost in predicting aeroacoustic feedback compared to DNC, we apply, according to Jones et. al [3] and Frank [5], a simple perturbation formulation. The following method can be easily implemented into the high-order method described above. The nonlinear Navier-Stokes operator reads as

$$U_t = R(U). \tag{5}$$

Inserting the Reynolds decomposition which reads as $U = U_0 + U'$ and rearranging the equation leads to

$$U'_t = R(U_0 + U') - R(U_0). \tag{6}$$

The second part of the right-hand side of Equation (6) represents the base flow time derivative. Subtraction of the former in each time step can be interpreted as a forcing back onto the baseflow. This method allows us to analyze the impulse response of a small perturbation to any provided baseflow, which is like a global stability analysis. The analysis of the obtained time series gives insight into the dynamics of the system and allows us to reveal acoustic feedback. Decomposing the time series into approximate global instability modes by applying a dynamic mode decomposition (DMD) reveals the least damped global instability mode which is associated to the characteristic acoustic feedback mode. The DMD algorithm used is based on Schmidt [14].

2.3. RANS solver

As stated in the previous section any baseflow can be chosen for the high fidelity perturbation analysis. This gives us the possibility to achieve an efficient method for predicting aeroacoustic feedback. In this work we choose the library OpenFOAM®, more precisely the simpleFoam solver, which is a steady-state solver for incompressible, turbulent flow, using the SIMPLE (Semi-Implicit Method for Pressure Linked Equations) algorithm. The algorithm solves the incomrpessible RANS equations using a finite volume (FV) method. A turbulence model is used for closure. Furthermore, the algorithm follows a segregated solution strategy meaning that the unknown variables, which are the velocity, pressure and the turbulence variabales, are solved sequentially. More information about the SIMPLE algorithm and the FV method can be found in Ferziger [15].

In this work the RANS equations are closed by the Langtry-Menter 4-equation transitional SST model. The model is given by the four equations for the turbulent kinetic energy, the specific turbulence dissipation rate, the intermittency and one for transition onset criterion in terms of momentum-thickness Reynolds number. The model coefficients are chosen to be equal to the default values as implemented into the OpenFOAM® release v1712. Details of this turbulence and transition model can be found in [16], [17] and [18].

2.4. Coupling strategy

This section is dedicated to explaining the strategy of the perturbation analysis applied in this work. As mentioned we can choose any baseflow for the perturbation analysis. Choosing the state-of-the art CFD-library OpenFOAM® for generating a suitable baseflow unavoidably leads to a consideration of different solution representations and file formats. The DGSEM relies on a tensor product of 1-D Lagrange polynomials for the solution representation, whereas OpenFOAM® follows the finite volume typical cell-centered solution representation. The basic idea for the coupling mechanism is derived from sub-cell methodes used for shock capturing procedures described e.g. by Sonntag [19]. Here, a DG reference element is split into equidistant FV sub-cells with the same amount of degrees of freedom, which is $(N + 1)^{2/3}$ for each cell in the two- respective three-dimensional case. The transformation between the DG and the FV sub-cell formulation describes the desired transfer from DG to FV and vice versa. By converting the FV sub-cell mesh into the OpenFOAM® native polymesh format, maintaining the original mesh structure, and computing the baseflow on this mesh allows us to easily transform the FV solution to the DG polynomials. To do so, the solution on the FV sub-cells in the physical space are transformed back into the reference element and the conversion is carried out. For a rectilinear grid this method can be directly applied. In this case the OpenFOAM® barycenters transformed to the reference element coincide with the barycenters of the FV sub-cells in the reference element. In case of skewed elements or even curved meshes the barycenters of the polymesh differ from the FV sub-cells due to the fact of different estimations of the barycenters. For this more general case a correction is carried out. To do so, the reference coordinates describing the physical coordinates of the polymesh barycenters within the reference element are searched with Newton's method. The correction is now applied by interpolating to the expected barycenters of the FV sub-cells using the Lagrange polynomials of degree N.

The proposed strategy offers quite a lot of flexibility. It is possible to overcome the restriction of only using hexahedra elements by carrying out the baseflow simulation on an arbitrary mesh and map the solution on the polymesh derived from the DG mesh. The presented coupling strategy is summarised in Figure 1.

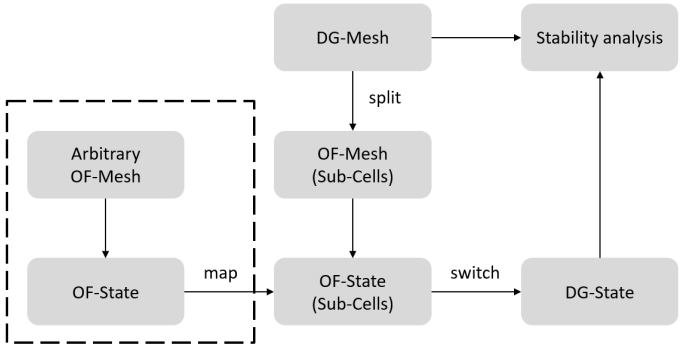

Figure 1: Coupling strategy between OpenFOAM® and FLEXI.

3. COMPUTATIONAL SETUP

The simplified side-view mirror model described by Frank [5] and Werner [20] is considered as a test example for the proposed method. This mirror is an abstraction

mimicking the pressure distribution of a real side-view mirror on which aeroacoustic feedback was detected. The defining feature was found to be the so called "design edge" on top of the modelwhich induces laminar separation. The length of the model is $C = 70.17\ mm$. A splitter plate, with length $L/C = 8$ is mounted central at the rear of the body to calm the wake. Without the splitter plate vortex shedding at low frequency can be observed which dominates the flow and no tonal noise component is present. We consider in the following two setups, the first one is used as validation of the second setup, which represents the new method presented here. The validation setup follows Frank [5] and consists of three steps. The first step is a baseflow LES of the whole domain followed by a well resolved submodel simulation, with boundary conditions enforced by the computed baseflow. The third step is carrying out the perturbation analysis on the time-averaged summodel simulation. To correctly represent the pressure distribution on the body surface it is crucial to depict the turbulence adequately. Therefore, the full domain simulation is carried out three-dimensional. The following submodel simulations, which are better resolved to capture the instability mechanism, are carried out two-dimensional in order to reduce computational cost, knowing from Jones et. al [3] and Frank [5] that a two-dimensional simulation is capable of depicting the feedback mechanism which is dominated by coherent two-dimensional flow structures.

The setup of the new method proposed follows step one and three. In the first step a well resolved time-averaged flow field is obtained by solving the RANS equations. Here, a two-dimensional simulation is executed directly to gain the baseflow. The second step, which is mapping the time-averaged flow field onto the submodel, transforming the FV-data to DG-polynomials and carrying out the perturbation analysis, is computed with DGSEM.

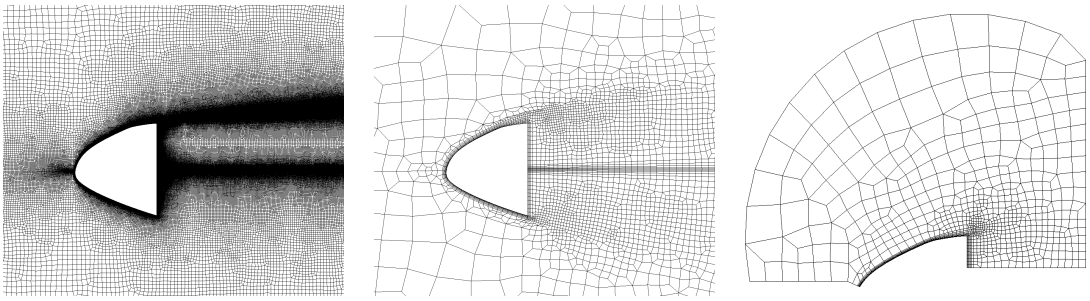

Figure 2: Computational meshes. Left: mesh of the RANS simulation, middle: mesh of the DG simulation, right: mesh used for the submodel simulation.

3.1. Baseflow

The baseflow simulation for the high order case is carried out a the baseline freestream velocity of $U_\infty = 27.78\ m/s$. A section of the grid used for computation is displayed in Figure 2 (middle). The domain is circular with radius $R = 100C$ and has a spanwise extend of $L_z = 42.1m$ for the three-dimensional simulation. The spanwise extend is chosen according to Frank [5] which has been shown to be large enough to prevent spanwise correlation. The grid comprises of approximately 122,000 elements and is discretized with 16 equidistant layers in spanwise direction. The polynomial degree of the DGSEM approximation is chosen to $N = 5$ and the geometry is represented by $N_{Geo} = 4$. This results in about 26.4 m. degrees of freedom. The grid spacings, defined as $\Delta[\cdot] = \Delta[\cdot]_{cell}/(N+1)$, evaluated at the design edge are the following: $\Delta x = 0.32\ mm$ and

$\Delta y = 0.036\ mm$. To suppress artificial reflections a circular sponge zone with radius $R/C = 20$ is placed around the body. In the spanwise direction periodic boundary conditions are applied.

For the new proposed approach baseflow simulations are carried out with a RANS solver. Several freestream velocities between $U_\infty = 10\ m/s$ and $U_\infty = 27.78\ m/s$ are computed. The computational grid is displayed in Figure 2 (left) and is based on the same circular domain as mentioned above. The grid is made up of about $856,000$ cells. The near wall region is fully resolved with a near wall grid resolution yielding $y^+ < 1$ on all surfaces. To ensure a smooth solution representation after switching to the polynomial solution representation, regions with expected high gradients are refined. By the use of a turbulence model we are able to conduct immediately a two-dimensional simulation.

3.2. Submodel

The setup of the submodel simulation is independent of the choice of the baseflow and will be carried out with the presented high order DGSEM. In order to reduce computational cost a two-dimensional submodel simulation is carried out. The grid of the submodel is displayed in Figure 2 (right). To capture the dynamics of the instability mechanism the resolution is increased by p-adaption, the polynomial degree is set to $N = 7$. The mesh resolution of the submodel region itself is comparable to the baseflow case. The vicinity of the boundary to the body requires careful treatment of the boundary conditions. The time average of the baseflow simulation provides the far field boundary conditions as well as the reference flow for the sponge region. This ensures a damping of the fluctuations towards the reference solution and prevents artificial reflections.

4. FULL MODEL SIMULATION

The discussion of the full model simulation is based on the baseline case of $U_\infty = 27.78\ m/s$. We want to compare the results based on the DGSEM method with the FV method. For validation we compare the results with the data published by Frank [5]. To compare the transient simulation with the steady state solution obtained from the RANS equations we average the transient data in time. For the transient simulation the flow field is initialized with the freestream velocity of $U_\infty = 27.78\ m/s$. Therefore, before time averaging the simulation is advanced for 20 convective time units $T^* = C/u_\infty$ and then averaged over $180T^*$. Comparison of the length of the recirculation bubble on the top of the splitter-plate shows in comparison to the time average of the resolved simulation that the RANS simulation underestimates the length of the recirculation bubble. The length of the time averaged solution is $L/C = 6.97$ compared to $L/C = 5.77$ of the RANS solution. The difference is attributed to the discrepancy between two-dimensional and three-dimensional simulation as well as differences in the resolution capabilities of the models used. The resulting influence on the pressure distribution on the upper side, on the other hand, is minor. In Figure 3 the pressure coefficient of the upper side of the model is plotted as well as the results of Frank [5]. Both simulations reflect the trend of the pressure distribution very well. The location of the suction peak match very well the location of the design edge at $X_{DE}/C = 0.67$. The RANS simulation overestimates the strength of the suction compared to the reference. This is accounted to the underestimation of the length of the recirculation bubble above the splitter plate. During the formation of the recirculation zone, it can be observed

that the pressure distribution on the upper side decreases as the recirculation zone grows larger. The suction peak is followed by a plateau of nearly constant pressure distribution, indicating the presence of a separation. Looking at the separation point, defined by change of sign of the wall shear stress, yields $X/C = 0.765$ for the high-fidelity simulation and $X/C = 0.763$ for the RANS simulation. A variation of the freestream velocity was carried out for the RANS simulation. The additional freestream velocities $U_\infty = 10\ m/s,\ 15\ m/s,\ 16.25\ m/s,\ 17.5\ m/s,\ 20\ m/s,\ 22.5\ m/s$ and $U_\infty = 25\ m/s$ were computed.

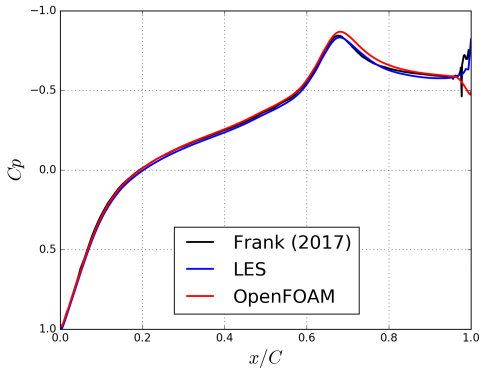

Figure 3: Time averaged pressure coefficient c_p on the mirror surface.

5. SUBMODEL SIMULATION

In the following the submodel simulation with the DGSEM for the baseline velocity $U_\infty = 27.78\ m/s$ is discussed. The submodel simulation is carried out acording to Section 3.2. As initial solution the time averaged solution of the full model is mapped to the sub model and chosen as a baseflow for the sponge zone as well as the far field boundary condition. At first the initial solution is advanced for $70T^*$. From there on the acoustic emissions at $X/C = 1, Y/C = 1.5$ are recorded as well as time averaging is performed. The time averaged flow field is used afterwards as baseflow for the perturbation analysis described in the next section. The resulting acoustic spectrum is displayed in Figure 4. Displayed is the pressure spectral density in comparison to the reference of Frank [5]. In the spectrum there is a dominant peak at about 2560 Hz. This peak is associated to the aeroacoustic feedback mechanism. In comparison to the results of Frank there is a slight shift to higher frequencies noticeable as well as a slight shift towards higher spectral density, but over all there is good agreement of the spectra. The results of the spectra of the direct noise computation should now be seen as the reference for validation of the perturbation analysis in the following section.

5.1. Perturbation analysis

Based on the full model simulation with the RANS solver and the time averaged flow field of the submodel simulation, we want to carry out the perturbation simulation on the submodel. We analyze the temporal dynamics of the impulse response triggered by the introduced disturbance with the DMD. We compare the results based on the two different baseflows and validate it against the direct simulation. Furthermore, we want to examine whether the dependence of the tonal frequency on the freestream velocity

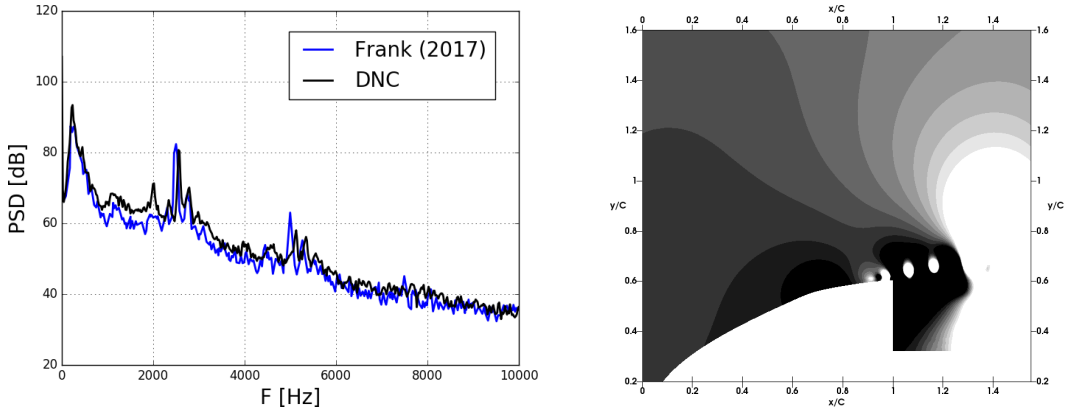

Figure 4: PSD of the pressure fluctuations at $(1, 1.5)$*,* $p_{ref} = 4 \cdot 10^{-10} Pa^2/Hz$ *(left). Pressure fluctuation* $p' = p - \langle p \rangle$ *contours (right).*

can be depicted by the proposed new method. For the perturbation analysis the equation described in Section 2.2 is solved by the DGSEM method. As an initial perturbation a sharp-edged perturbation, in order to excite a wide range of wavelengths, with amplitude of 10^{-8} is introduced into the initial momentum und density field. In Figure 5 the pressure fluctuation within the near wall boundary triggered by the introduced perturbation is shown. In this case the baseflow was computed with the RANS solver. The figure reveals two effects. At first the wave packet, triggered by the perturbation, travels downstream. The triggered hydrodynamic wave packets are dominant on the rear of the geometry. The second effect is the acoustic wave travelling upstream with lower amplitude in comparison. The figure further shows a stable feedback loop meaning the upstream travelling acoustic waves trigger new wave packages with increasing amplitude.

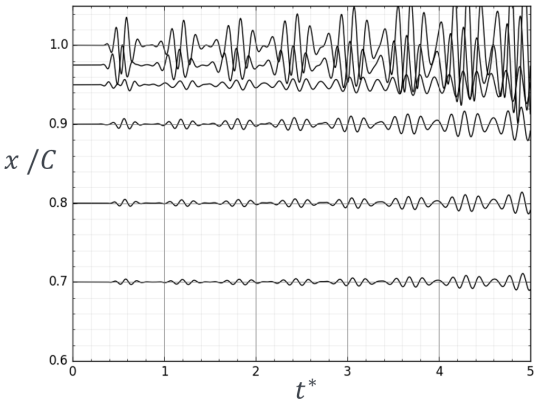

Figure 5: Pressure fluctuations plotted within the boundary layer (arbitrary amplitude).

In the following the associated time series is analyzed by the means of a DMD. A time series of $5T^*$ with $\Delta t = 0.01$ is analyzed. The results are presented in Figure 6. Besides the presented perturbation analysis, the perturbation analysis of the reference simulation is presented, which in the following will be referred as the reference. In the diagram you can see the real part plotted over the imaginary part of the complex eigenvalues ω which are associated to the growth rate and the angular frequency of the mode. The color and size of the plotted modes are encoded with the Euclidean norm of the respective mode which can be seen as a measure of energy of the modes.

Direct comparison of both results shows good agreement in terms of matching

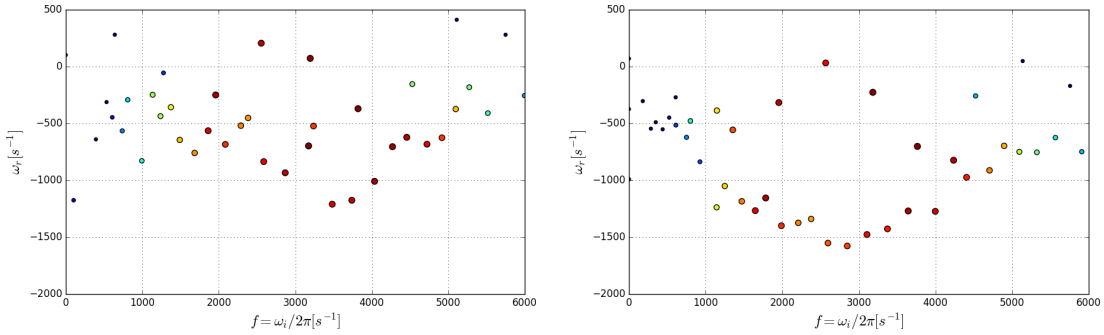

Figure 6: Spectrum of Ritz values delivered by the DMD algorithm based on the perturbation simulation in the time interval $0 \leq t \leq 5$. Size and color coding indicate the Euclidean norm of the respective mode. Left: baseflow computed with DGSEM, right: baseflow computed with RANS.

frequencies of the dominant modes. A slight shift towards higher growth rates is noticeable for the new approach. This indicates a dominant influence of the geometry to the frequency selection and a great influence of the detailed boundary layer properties towards predicting the physical damping rate. In Table 1 the frequencies of the least damped energetic modes as well as the adjacent modes are listed. Compared to the dominant tonal frequency found in DNC at $f = 2550\ Hz$, the results of the DMD are in good agreement with the dominant frequency found in the perturbation analysis. Compared to the results published by Frank [5] the same frequency shift was found as in the DNC, but comparison of the deltas of the adjacent frequencies demonstrates again good agreement.

$f\ [Hz]$	M1	**M2**	M3
Reference	1956	**2567**	3183
New approach	1959	**2555**	3195
Frank [5]	1917	**2525**	3145

Table 1: Dominant frequencies obtained from DMD.

Those promising results for the baseline velocity shows great potential of the new proposed method. In the following we want to present the results of the variation of the freestream velocities. In Table 2 the frequencies of the least damped modes found by DMD of the perturbation analysis are listed. For comparison the tonal frequencies found by frank with DNC are listed as well. The overall trend is reproduced well. Towards lower velocities the deltas of the frequencies increase slightly to a maximum difference of 66 Hz. For the case of $U_\infty = 10\ m/s$ the mode structure as seen in Figure 6 collapses and no mode which would refer to an aeroacustic feedback mode is present. The corresponding spectra provided by Frank doesn't show any peak frequency as well.

$f\ [Hz]$	$10\ m/s$	$15\ m/s$	$16.25\ m/s$	$17.5\ m/s$	$27.78\ m/s$
Perturbation analysis	-	1440	1570	1680	2555
Frank, DNC [5]	-	1506	1633	1720	2519

Table 2: Comparison of the feedback frequencies found by perturbation analysis with DNC results of Frank [5] for a variation of the freestream velocity.

6. CONCLUSIONS

The present work deals with an efficient method to capture aeroacoustic feedback induced by the flow around a side-view mirror. Based on a simplified geometry, that has already been investigated intensively for feedback, a global perturbation ansatz based on a baseflow obtained from a RANS solver is proposed. The potential of the stability analysis has been demonstrated in the past by Jones et. al [3] and Frank [5], with the downside of computationally expensive time averaging of transient LES or DNS to obtain the baseflow. Through the use of a RANS solver to compute the baseflow the computational effort reduces significantly.

A direct simulation was carried out at the baseline velocity of $U_\infty = 27.78\ m/s$ to have an acoustic spectrum for validation as well as to be used as a reference baseflow in order to obtain a reference perturbation analysis. Conducting a two-dimensional perturbation analysis of a sudmodel based on the RANS baseflow as well as the reference baseflow, followed by a dynamic mode decomposition reveals the selection of discrete frequencies by the mechanism. There was found good agreement of the least damped modes with the tonal frequency found by DNC as well as the literature. This leads to the conclusion that RANS simulations are suitable as baseflow for a high order disturbance analysis. To summaries, the proposed method is a first step to facilitate the prediction of aeroacoustic feedback in an industrial context.

7. ACKNOWLEDGEMENTS

We thank the AUDI AG for their financial support. This work used HPC resources on the CRAY XC40 hazelhen at the High Performance Computing Center Stuttgart (HLRS).

8. REFERENCES

[1] Robert W. Paterson, Paul G. Vogt, Martin R. Fink, and C. Lee Munch. Vortex noise of isolated airfoils. *Journal of Aircraft*, 10(5):296–302, 1973.

[2] Henri Arbey and J. Bataille. Noise generated by airfoil profiles placed in a uniform laminar flow. *Journal of Fluid Mechanics*, 134:33–47, 1983.

[3] Lloyd E. Jones and Richard D. Sandberg. Numerical analysis of tonal airfoil self-noise and acoustic feedback-loops. *Journal of Sound and Vibration*, 330(25):6137–6152, 2011.

[4] Todd H. Lounsberry, Mark E. Gleason, and Mitchell M. Puskarz. Laminar flow whistle on a vehicle side mirror. Technical report, SAE Technical Paper, 2007.

[5] Hannes Frank. High order large eddy simulation for the analysis of tonal noise generation via aeroacoustic feedback effects at a side mirror. *Dr. Hut, München*, 2017.

[6] Florian Hindenlang, Gregor J. Gassner, Christoph Altmann, Andrea Beck, Marc Staudenmaier, and Claus-Dieter Munz. Explicit discontinuous galerkin methods for unsteady problems. *Computers & Fluids*, 61:86–93, 2012.

[7] David A. Kopriva. Metric identities and the discontinuous spectral element method on curvilinear meshes. *Journal of Scientific Computing*, 26(3):301, 2006.

[8] David A. Kopriva. *Implementing spectral methods for partial differential equations: Algorithms for scientists and engineers*. Springer Science & Business Media, 2009.

[9] Eleuterio F. Toro. *Riemann solvers and numerical methods for fluid dynamics: a practical introduction*. Springer Science & Business Media, 2013.

[10] Francesco Bassi and Stefano Rebay. A high-order accurate discontinuous finite element method for the numerical solution of the compressible navier–stokes equations. *Journal of computational physics*, 131(2):267–279, 1997.

[11] Mark H. Carpenter and Christopher A. Kennedy. *Fourth-order 2N-storage Runge-Kutta schemes*. Technical Report, NASA-TM-109112, 1994.

[12] Dave Pruett, Thomas Gatski, Chester Grosch, and William Thacker. The temporally filtered Navier-Stokes equations: properties of the residual stress. *Physics of Fluids*, 15(8):2127–2140, 2003.

[13] David Flad, Hannes Frank, Andrea Beck, and Claus-Dieter Munz. A discontinuous Galerkin spectral element method for the direct numerical simulation of aeroacoustics. *AIAA Paper (2014-2740)*, 2014.

[14] Peter J. Schmid. Dynamic mode decomposition of numerical and experimental data. *Journal of fluid mechanics*, 656:5–28, 2010.

[15] Joel H. Ferziger and Milovan Peric. *Computational methods for fluid dynamics*. Springer Science & Business Media, 2012.

[16] Florian R. Menter. Two-equation eddy-viscosity turbulence models for engineering applications. *AIAA journal*, 32(8):1598–1605, 1994.

[17] Florian R. Menter, Martin Kuntz, and Robin Langtry. Ten years of industrial experience with the sst turbulence model. *Turbulence, heat and mass transfer*, 4(1):625–632, 2003.

[18] Robin B. Langtry and Florian R. Menter. Correlation-based transition modeling for unstructured parallelized computational fluid dynamics codes. *AIAA journal*, 47(12):2894–2906, 2009.

[19] Matthias Sonntag and Claus-Dieter Munz. Shock capturing for discontinuous galerkin methods using finite volume subcells. In *Finite Volumes for Complex Applications VII-Elliptic, Parabolic and Hyperbolic Problems*, pages 945–953. Springer, 2014.

[20] Maike Werner. Experimental study on tonal self-noise generation by aeroacoustic feedback on a side mirror, 2018. viii, 133 Seiten.

[21] Leo L. Beranek and István L. Vér. *Noise and Vibration Control Engineering – Principles and Applications*. John Wiley & Sons, New York, 2006.

[22] Lothar Cremer, Manfred Heckl, and Björn Petersson. *Structure-Borne Sound - Structural Vibrations and Sound Radiation at Audio Frequencies*. Springer, 2005.